

Efficient and robust 3D blind harmonization for large domain gaps

Hwihun Jeong^{1,2} Hayeon Lee¹ Se Young Chun^{1,3} Jongho Lee¹

¹Department of ECE, ³INMC & IPAI, Seoul National University

²BWH, Harvard Medical School

{hwihuni, hiyeon, sychun, jonghoyi}@snu.ac.kr

Abstract

Blind harmonization has emerged as a promising technique for MR image harmonization to achieve scale-invariant representations, requiring only target domain data (i.e., no source domain data necessary). However, existing methods face limitations such as inter-slice heterogeneity in 3D, moderate image quality, and limited performance for a large domain gap. To address these challenges, we introduce BlindHarmonyDiff, a novel blind 3D harmonization framework that leverages an edge-to-image model tailored specifically to harmonization. Our framework employs a 3D rectified flow trained on target domain images to reconstruct the original image from an edge map, then yielding a harmonized image from the edge of a source domain image. We propose multi-stride patch training for efficient 3D training and a refinement module for robust inference by suppressing hallucination. Extensive experiments demonstrate that BlindHarmonyDiff outperforms prior arts by harmonizing diverse source domain images to the target domain, achieving higher correspondence to the target domain characteristics. Downstream task-based quality assessments such as tissue segmentation and age prediction on diverse MR scanners further confirm the effectiveness of our approach and demonstrate the capability of our robust and generalizable blind harmonization.

1. Introduction

Magnetic resonance imaging (MRI) is a widely used medical imaging technique that provides detailed information of soft tissues. Recently, deep learning has been applied to MRI for various tasks, including disease classification [3, 26, 41], tumor segmentation [2, 53], and solving inverse problems [21, 50]. However, the effectiveness of deep learning in MRI is often limited by a challenge: a domain gap in MRI data. Variations can occur in MR images due to differences in scanner vendors, settings, or protocols, even when imaging the same patient. This variability creates domain gaps and hinders the performance of a neural network

trained on datasets with a different domain. To address these challenges, researchers have developed several harmonization methods to align source domain images (i.e., images with domain gaps) with the characteristics of the target domain. These methods include both traditional techniques [17, 32, 35, 38, 42, 43] and deep learning approaches [4, 12, 13, 15, 19, 30, 33, 47].

While these harmonization methods have shown promising results particularly when using deep learning-based methods, they typically require both source and target domain data for network training, still limiting generalization to unseen source domains. To address this challenge, the concept of “blind harmonization” has recently been proposed [23]. This approach enables the training of a harmonization network using only target domain data while allowing generalization to unseen source domain images. For example, BlindHarmony [23] utilizes an unconditional flow model trained exclusively on target domain data and produces a harmonized image that maintains a correlation with the input source domain image. This technique does not require source domain data during training.

Despite this unique advantage, several limitations exist (Fig. 1a). First, the previously proposed methods [5, 23] struggle to harmonize source domain images with a large domain gap. Second, the normalizing flow models primarily functioned as image density estimators rather than image generators, due to the inherent limitations in the expressiveness of normalizing flows. This constraint necessitates iterative processes for image generation, impeding the computationally efficient creation of high-quality harmonized images. Lastly, current blind harmonization models are restricted to 2D image generation, which can lead to inter-slice heterogeneity when applied to a 3D volume.

Recently, efforts [29, 31, 40, 46] were made to reduce sampling times in the diffusion model, enabling practical application. Among these, rectified flow [29] learns a transport map between two arbitrary distributions, streamlining the generation process while maintaining high image quality. Furthermore, a few studies [6, 10, 18, 24, 28, 45] explore the training of diffusion models particularly for 3D

image generation. However, training with large 3D volumes remains a challenge due to the limitations of computational resources, which typically confine processing to smaller 3D volumes (*e.g.*, patch-based training).

In this paper, we propose BlindHarmonyDiff, a novel 3D blind harmonization framework based on the edge-to-image model that was introduced in a few previous edge-conditioned image generation methods [9, 48, 51]. Our approach leverages the observation that MR images of the same subject, despite varying contrasts due to different acquisition settings, maintain consistent edge information. Building on this insight, we develop an edge-to-image model trained for target domain data to reconstruct the original image from the edge map detected by an edge-detection method. For inference, we apply the same edge detection method to a source domain image and input the resulting edge map into our trained model to generate a harmonized image. Moreover, unlike previous edge-conditioned image generation methods, we enable 3D generation with advanced 3D patch training and suppress hallucination using a refinement module with domain knowledge. Our key contributions are:

1. We present a novel 3D harmonization framework that utilizes an edge-to-image model designed for harmonization tasks.
2. Multi-stride patch methodology is proposed for efficient 3D model training, enhancing the ability to capture and generate 3D volumetric structures.
3. To mitigate hallucination and ensure robust inference, we propose a refinement module that enforces physical consistency between source and target domain images.

2. Related works

2.1. MRI harmonization

Several studies have developed techniques for harmonizing MR images between source and target domains. Traditionally, these methods have utilized image-level post-processing techniques, such as histogram matching [35, 36, 42] and statistical normalization [17, 38, 43]. However, these conventional methods often struggle to capture subtle differences between images from distinct domains. The advent of deep learning has led to advancements in harmonization methods. One notable approach is DeepHarmony [12], which employs an end-to-end supervised learning framework to establish mappings between source and target domains. However, it necessitates large datasets of traveling subjects, which can be challenging to be acquired. To overcome this limitation, researchers have turned to CycleGAN-based style transfer networks [30, 33], which can learn mappings between images from different domains without requiring paired data. Moreover, recent developments have introduced separate networks for contrast and

structure [7, 13, 55], allowing for greater flexibility in harmonization tasks. Recently, blind harmonization methods [5, 23] have been proposed to harmonize images from an unseen source domain by leveraging a normalizing flow model trained exclusively on a target domain dataset.

2.2. Patch-based training for diffusion models

Studies have aimed to reduce the high training costs of diffusion models through patch-based training. Patch-DM [14] is one of such methods with feature collage techniques in feature space to avoid boundary artifacts when generating large-size images. PatchDDM [6] utilizes fixed-size patches with coordinate encoding to reduce memory consumption during training. Patch Diffusion [49] employs diverse patch sizes to capture cross-region dependencies at multiple scales, enhancing data efficiency, especially for smaller datasets. Both PatchDDM and Patch Diffusion use pixel-level coordinates and full-size inference to avoid boundary artifacts. However, PatchDDM overlooks capturing global dependencies due to fixed patch sizes, and Patch Diffusion focuses on 2D training and does not reduce memory usage, limiting large 3D data processing.

3. Methods

3.1. Harmonization model

The BlindHarmonyDiff framework is based on the assumption that MR images of the same subject acquired with different settings (*e.g.*, vendor, scanner, parameters) exhibit varying contrasts but maintain a consistent edge [23]. Then, the construction of the target domain image (x_{tar}) and source domain image (x_{src}) of the same subjects can be formulated as below:

$$x_{tar} = I(e, C_{tar}), x_{src} = I(e, C_{src}), \quad (1)$$

where I is the image generation function from an edge and contrast, e is a common edge, and C_{tar}, C_{src} are the contrasts of the target and source domain image, respectively. This allows the edge detection method (D) to produce the same edge map from the target domain image (x_{tar}) and source domain image (x_{src}).

$$D(x_{tar}) = D(x_{src}) = e. \quad (2)$$

Leveraging this assumption, we developed an edge-to-image model ($E2I$) trained to reconstruct an original image from its edge map, which was detected using an edge detection method applied to the target domain image (Fig. 1b).

$$\theta^* = \arg \min_{\theta} \mathcal{L}(E2I(D(x_{tar}), \theta), x_{tar}), \quad (3)$$

where θ represents parameters of the edge-to-image model and \mathcal{L} is a loss function for training. Using these facts, we

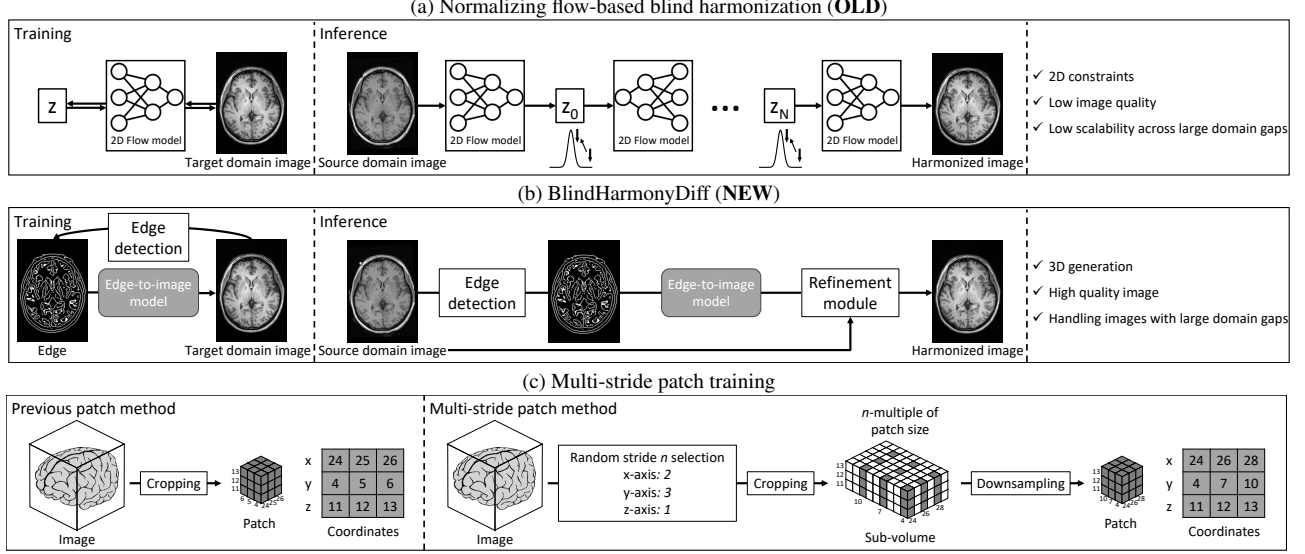


Figure 1. (a) Previous blind harmonization methods have limitations such as 2D reconstruction, moderate image quality, and limited performance for a large domain gap. (b) BlindHarmonyDiff is a 3D blind harmonization method designed to overcome the limitations of the previous methods. BlindHarmonyDiff trains an edge-to-image model only with the target domain image and generates a harmonized image by inputting an edge map from the source domain image into the trained model. A refinement module then enhances the harmonized image to maintain a high correlation with the input source domain image. (c) An edge-to-image model is trained with a newly proposed multi-stride patch processing. As compared to a previous patch method, which simply creates a patch from neighboring voxels of an image, a multi-stride patch method randomly selects strides to construct a patch.

can harmonize the source domain image to the target domain by detecting the edge of the source domain image to unlearn the contrast of the source domain and then reconstructing the contrast of the target domain with the trained edge-to-image model:

$$x_{har} = E2I(D(x_{src}), \theta^*), \quad (4)$$

where x_{har} is the resultant harmonized image (Fig. 1b).

3.2. Edge detection method

We employ Canny edge detection [8] as an edge detection method. To ensure consistent edge detection across different subjects and domains, we implement a subject-level Canny edge detection threshold determination approach. This approach maintains a uniform ratio of edge voxels to total image voxels. The algorithm iteratively adjusts the Canny edge detection threshold: if the ratio of edge voxels to total image voxels exceeds the predetermined value, the threshold is decremented. Through this process, we establish the Canny edge detection threshold that consistently yields 8% edge voxels relative to the total image voxels.

3.3. Patch-based rectified flow

For training the edge-to-image model, we utilize coordinate-encoded patch-based diffusion model training strategies [6, 49], enabling efficient 3D training with limited resources and allowing inference for an entire 3D

volume to avoid boundary artifacts. Our goal is to train a 3D patch-based edge-to-image model via rectified flow [29], which connects an image patch (x_1) and a Gaussian noise (x_0) on a straight trajectory:

$$dx_t = v(x_t, t) dt, \quad \text{where } x_t = tx_1 + (1-t)x_0, \quad (5)$$

where v represents the velocity field, parameterized as a neural network using the corresponding edge map patch (e). Spatial coordinates (i, j, k) are derived from the full images and normalized to range from -1 to 1, encoding positional information for each axis. The edge map patch (e) and positional coordinates (i, j, k) are used as conditions to control the rectified flow process. With the conditions (e, i, j, k) , the velocity field (v_θ) is optimized by minimizing the following loss function:

$$\mathcal{L} = \mathbb{E}_{x_0 \sim \mathcal{N}(0,1)} \left[\int_0^1 \|(x_1 - x_0) - v_\theta(x_t, t; e, i, j, k)\|^2 dt \right]. \quad (6)$$

3.4. Multi-stride patch

We propose a novel multi-stride patch approach (Fig. 1c), which introduces a new way to generate patches for patch-based training. Unlike previous methods that extract patches with a fixed size (e.g., 64^3), our approach first randomly crops the whole 3D volume into a sub-volume with an n -multiple of the fixed patch size (e.g., $128 \times 192 \times 64$,

corresponding to $2\times$, $3\times$, and $1\times$ of 64^3 , respectively). The sub-volume is then downsampled to the fixed patch size. To embed spatial context, we adjust and concatenate positional coordinates with the patches. This strategy maintains memory efficiency while effectively capturing cross-region dependencies, providing a coherent representation of global structures within the 3D data.

3.5. Refinement module

To address the potential hallucination issue inherent in diffusion models and enhance the reliability of harmonized images, we implement a refinement module applied to the edge-to-image model output. Because the difference between the source domain image and the target domain image primarily exists in the low-frequency region, the two images exhibit high correlation [23]. Leveraging this insight, we construct the refinement module by increasing the subject-wise normalized cross-correlation between the harmonized image and the input source domain image. Starting from the edge-to-image model output, the module performs gradient ascent, iteratively calculating the normalized cross-correlation between the source and generated images (step size = 0.02, the number of total iterations = 6; Fig. 1b).

4. Experiments and results

4.1. Dataset

T_1 -weighted images from the OASIS3 dataset [27] were used to train and evaluate the proposed framework. The OASIS3 dataset comprises images acquired using various scanners. We designated images scanned with the Siemens 3T Trio Tim scanner as the target domain. For the source domain, we employed four distinct datasets (1.5T Sonata, 3T BioGraph, 1.5T Vision, and 3T Magnetom Vida), each consisting of images acquired with different manufacturer models (details provided in Supplementary material S2). All images underwent resampling to a resolution of $1.2\times 1.2\times 1.25\text{ mm}^3$. We applied image normalization using subject-level percentile-based min-max normalization, considering the 1st to 99th percentiles.

4.2. Network training

The 3D edge-to-image model was trained on cubic patches of size 64^3 with a batch size of 8. The learning rate was set to 0.00005, and the Adam optimizer was employed. The training was conducted for 150K steps. The model architecture was based on a U-Net [39] with five input channels: one for Gaussian noise, one for the grayscale input, and three for the positional encoding of 3D coordinates (See Supplementary material S3 for detailed information).

4.3. Patch training for edge-to-image model

We implemented a multi-stride patch training approach for the 3D edge-to-image model. Multi-stride patches were

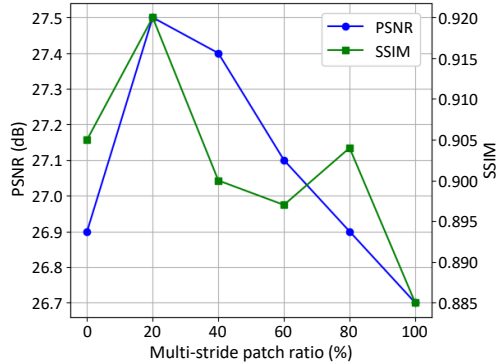


Figure 2. PSNR and SSIM across different multi-stride patch ratios. The ratio of multi-stride patches used in training ranged from 0% to 100% at 20% intervals.

generated by efficiently downsampling sub-volumes to a fixed patch size via indexing, avoiding computationally expensive methods such as linear interpolation. During training, multi-stride patches (sampled with strides greater than 1) were used together with simple patches (sampled at a stride of 1), enabling the model to effectively learn both local and global features. To determine the optimal ratio of multi-stride patches, we progressively increased their proportion from 0% to 100% during training. The performance of the edge-to-image model was evaluated across different ratios of multi-stride to simple patches using the target domain images (see Section 4.1). PSNR and SSIM metrics were calculated relative to the original image to assess performance.

Our experimental results (Fig. 2) demonstrate that the 20-80 split between multi-stride and simple patches produces the best PSNR and SSIM values. When compared to the simple patch training (*i.e.*, 0% in Fig. 2), PSNR increased from 26.9 dB to 27.5 dB, and SSIM improved from 0.905 to 0.920. Multi-stride patch effectively balances local and global feature learning, leading to improved performance compared to simple patch training. The results hereafter are obtained with the edge-to-image model trained with a 20-80 split.

4.4. Image level evaluation

To evaluate the performance of harmonization, we utilized traveling subjects with data acquired across multiple scanners. Images from four source domains were registered to the target domain images using FSL FLIRT [22]. The comparative analysis encompassed DeepHarmony [12], paired style transfer [30, 33], and several blind harmonization techniques including normalizing flow-based blind harmonization (BlindHarmony) [23], spectrum swapping-based image-level MRI harmonization (SSIMH) [20], and histogram matching. For SSIMH implementation, we aver-

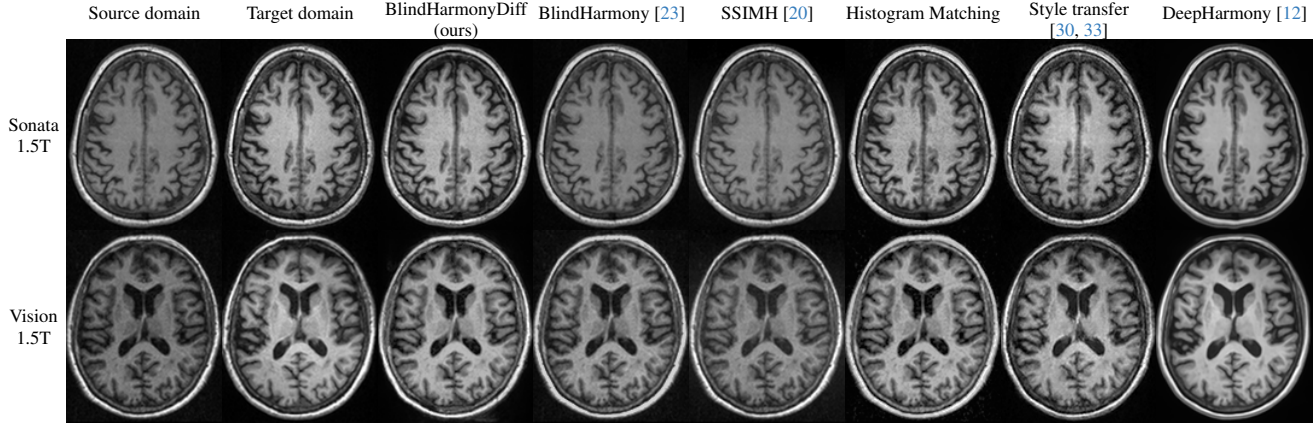


Figure 3. Visual comparison of harmonization results on traveling subjects, demonstrating the effectiveness of BlindHarmonyDiff against the other blind harmonization methods.

	Blind	Sonata 1.5T		BioGraph 3T		Vision 1.5T		Magnetom Vida 3T	
		SSIM(\uparrow)	PSNR(\uparrow)						
Source domain		0.810	18.6	0.842	20.0	0.601	14.5	0.816	18.2
BlindHarmonyDiff (ours)	O	0.908	23.4	0.862	23.3	0.697	19.3	0.851	21.3
BlindHarmony [23]	O	0.802	18.9	0.850	21.3	0.665	17.2	0.822	19.0
SSIMH [20]	O	0.817	19.8	0.855	22.3	0.656	17.7	0.836	20.3
Histogram matching	O	0.894	21.8	0.857	22.9	0.678	18.6	0.844	20.7
Style transfer [30, 33]	X	0.895	24.3	0.864	23.5	0.667	19.2	0.855	22.7
DeepHarmony [12]	X	0.932	25.2	0.909	25.4	0.897	25.0	0.881	21.3

Table 1. Quantitative assessment using PSNR and SSIM metrics, calculated relative to the target domain images. Results highlight the superior performance of BlindHarmonyDiff, reporting the best scores across the scanners.

aged the whole image of target domain images and replaced the low-frequency components of source domain images with the averaged target domain images using a 3D discrete cosine transform. Histogram matching was performed by storing the histogram of target domain images and matching the source domain image histogram to the target domain histogram at the subject level.

Figure 3 demonstrates the harmonization of the source domain image (column 1) to the target domain (column 2) using various harmonization methods. BlindHarmonyDiff (column 3) successfully harmonizes the source domain image, generating results with contrast similar to the target domain images. Compared to other blind harmonization methods (columns 4-6), BlindHarmonyDiff exhibits superior harmonization performance. While style transfer and DeepHarmony may demonstrate powerful harmonization capabilities, they are not blind harmonization methods, as their networks are trained on specific source domains.

Quantitative evaluation involves the calculation of PSNR and SSIM between harmonized and target domain images. The brain mask was extracted with FSL BET [44] and utilized for metric calculation. Table 1 presents PSNR and SSIM values between the target domain image and harmonized images produced by each method. The “Source

domain” row represents the source domain image without harmonization. Results demonstrate improved PSNR and SSIM metrics after applying BlindHarmonyDiff, with values comparable to those of style transfer methods trained for each source domain (average PSNR increase from 18.4 dB to 22.2 dB). Our method outperforms other blind harmonization techniques, including BlindHarmony, Histogram matching, and SSIMH, in both PSNR and SSIM metrics.

Normalizing flow-based blind harmonization exhibits lower PSNR and SSIM values compared to histogram matching and SSIMH. This discrepancy may be attributed to the differences in processing approaches: SSIMH and histogram matching were computed at the subject level using 3D processing, whereas BlindHarmony operated at the slice level with 2D processing. In the 2D case, BlindHarmony outperforms other blind harmonization methods, which is consistent with the previous results. (See Supplementary material S4)

4.5. Downstream task level evaluation

To evaluate the functional performance of harmonization, we adopted two downstream tasks: brain tissue segmentation and age prediction. Task networks were trained on the target domain dataset, resulting in performance degradation when source domain images were input due to the

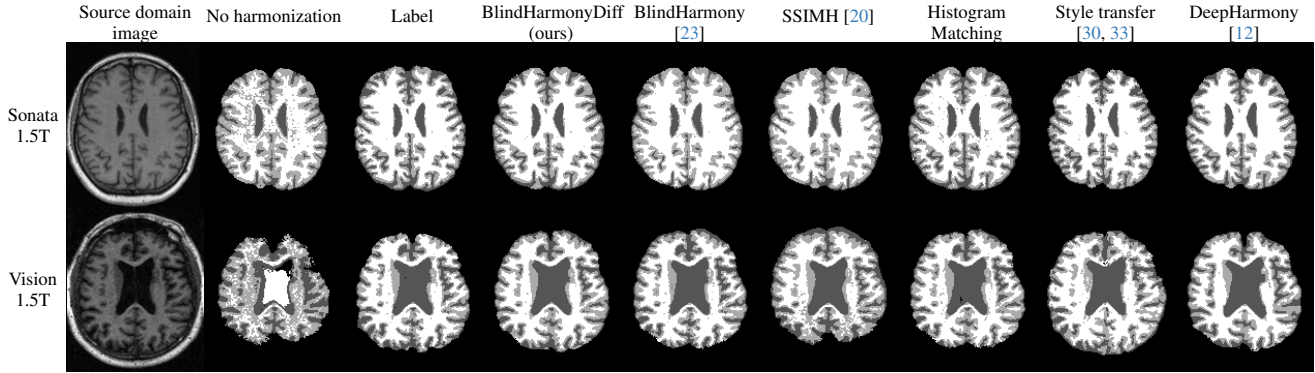


Figure 4. Tissue segmentation results for the various harmonization methods, with the segmentation network trained on the target domain data. Each column represents a different harmonization approach applied to the input images.

	Blind	Tissue segmentation: Dice(\uparrow)				Age prediction: MAE(\downarrow)			
		Sonata	BioGraph	Vision	Vida	Sonata	BioGraph	Vision	Vida
No harmonization		0.801	0.870	0.656	0.837	6.31	5.02	15.4	4.78
BlindHarmonyDiff (ours)	O	0.879	0.872	0.806	0.846	5.60	4.91	6.94	4.63
BlindHarmony [23]	O	0.778	0.846	0.752	0.825	5.80	4.96	12.6	5.39
SSIMH [20]	O	0.755	0.866	0.748	0.837	6.65	5.17	13.2	5.18
Histogram matching	O	0.869	0.865	0.793	0.835	6.19	5.08	10.5	5.34
Style transfer [30, 33]	X	0.807	0.851	0.697	0.804	8.38	5.51	6.74	6.10
DeepHarmony [12]	X	0.820	0.757	0.626	0.765	5.15	7.70	6.41	10.2

Table 2. Evaluation of the methods for two downstream tasks: tissue segmentation and age prediction. Quantitative assessments were performed using a Dice score for the tissue segmentation and a mean absolute error (MAE) value for the age prediction. BlindHarmonyDiff demonstrates overall superior performance in reducing domain gaps in both tasks.

domain gap. Successful harmonization should bridge this gap, potentially improving downstream task performance. We generated brain tissue masks using FSL FAST [52] and obtained age information from the OASIS 3 dataset demographics [27]. For the segmentation network, we employed U-Net [39], while a CNN architecture similar to that used in [11] was implemented for age prediction.

Figure 4 presents tissue segmentation results using various harmonization methods. BlindHarmonyDiff (column 4) effectively reduces the domain gap between source and target domains, as evidenced by improved tissue segmentation accuracy compared to the non-harmonized case (column 2). Furthermore, BlindHarmonyDiff outperforms other harmonization methods, yielding segmentation results that closely align with the labels.

Table 2 presents the quantitative assessment for downstream tasks, including Dice scores for tissue segmentation and mean absolute errors (MAE) for age prediction. BlindHarmonyDiff demonstrates superior Dice scores for tissue segmentation and lower MAE for age prediction compared to other blind harmonization methods, confirming its robust harmonization capabilities. Notably, in tissue segmentation, BlindHarmonyDiff outperforms DeepHarmony, which was trained on each source domain image. This superior performance may be attributed to the blurred output of the U-Net

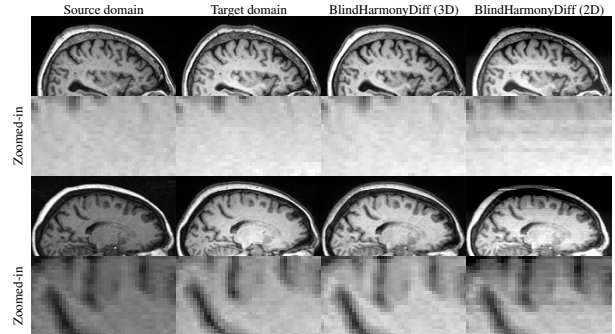


Figure 5. Comparison of 3D vs. 2D image processing networks. 2D processing shows inter-slice discontinuities (see zoomed-in image), while 3D processing yields homogeneous results across slices.

in DeepHarmony.

4.6. 3D vs. 2D in harmonization performance

To evaluate the effectiveness of our subject-wise 3D harmonization, we compared the results of 2D and 3D processing. For 2D processing, we trained the 2D rectified flow model at the slice level and calculated the slice-wise normalized cross-correlation in the refinement module.

Figure 5 presents exemplary results comparing 3D and

	Sonata 1.5T		BioGraph 3T		Vision 1.5T		Magnetom Vida 3T	
	SSIM(\uparrow)	PSNR(\uparrow)						
BlindHarmonyDiff (3D)	0.908	23.4	0.862	23.3	0.697	19.3	0.851	21.3
BlindHarmonyDiff (2D)	0.881	21.1	0.840	21.6	0.681	18.5	0.818	19.6

Table 3. Quantitative assessment for the comparison between 3D and 2D processing.

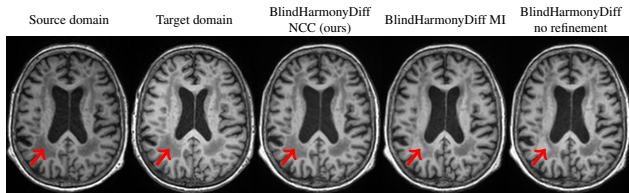


Figure 6. Impact of the refinement module on hallucination mitigation. Without the refinement module, BlindHarmonyDiff removes a lesion (fifth column; red arrows), demonstrating hallucination. The refinement module effectively alleviates this issue, (third column; red arrows) producing more reliable images.

Refinement module	Sonata 1.5T		BioGraph 3T		Vision 1.5T		Magnetom Vida 3T	
	SSIM(\uparrow)	PSNR(\uparrow)						
NCC	0.908	23.4	0.862	23.3	0.697	19.3	0.851	21.3
MI	0.877	22.6	0.836	22.4	0.693	19.2	0.827	21.1
None	0.870	22.3	0.827	22.1	0.689	19.1	0.820	20.9

Table 4. Quantitative ablation results show that the full BlindHarmonyDiff with normalized cross-correlation (NCC) outperforms versions with mutual information (MI) or without refinement module.

2D processing. The 3D approach yields more homogeneous results, effectively eliminating inter-slice discontinuities present in 2D processing (See zoomed-in image). Quantitative analysis (Table 3) further confirms the superior performance of 3D processing over 2D. This superiority may be attributed to the 3D rectified flow’s ability to learn inter-slice relationships and the refinement module’s consideration of whole-brain correlation information.

4.7. Refinement module test and Ablation study

To assess the contribution of the refinement module, we compared three options: BlindHarmonyDiff with normalized cross-correlation (BlindHarmonyDiff NCC; proposed), BlindHarmonyDiff with mutual information (BlindHarmonyDiff MI), and BlindHarmonyDiff without refinement module (BlindHarmonyDiff no refinement). For BlindHarmonyDiff MI, we updated the harmonized image using gradient ascent with mutual information between histograms of the harmonized and source domain images. We employed kernel density estimation [37] with a Gaussian kernel (256 bins, $\sigma = 0.01$) to calculate continuous histogram functions.

The refinement module proves crucial in reducing hallucination and preserving lesion information (Fig. 6; column 3 vs. column 5). Comparing normalized cross-correlation

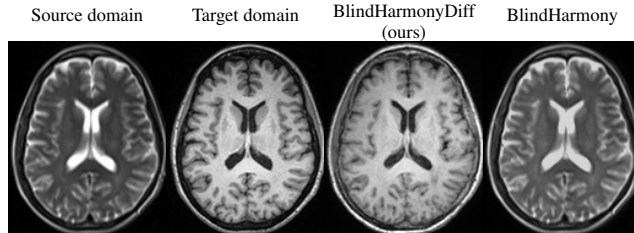


Figure 7. Evaluation of BlindHarmonyDiff in bridging a large domain gap (converting T₂-weighted image to T₁-weighted image) and comparison to the result of the original BlindHarmony.

and mutual information as refinement functions, the former demonstrates superior performance in preserving lesion information (Fig. 6; column 3 vs. column 4). We believe that it is due to NCC’s direct computation in the image domain, as opposed to MI’s calculation in the histogram domain. Quantitative analysis (Table 4) further confirms that the original BlindHarmonyDiff outperforms variants using mutual information or lacking a refinement module.

For the ablation study results testing the case without edge-to-image model, see Supplementary material S4.

4.8. Contrast conversion test

To explore the feasibility of applying blind harmonization to contrast conversion (e.g., T₂- to T₁-weighted images), we applied BlindHarmonyDiff, trained on T₁-weighted images, to T₂-weighted images. Due to the expected low correlation between T₁- and T₂-weighted images, we excluded the refinement module in this application.

Figure 7 demonstrates the result of applying BlindHarmonyDiff for T₂- to T₁-weighted image conversion. BlindHarmonyDiff exhibits capability in handling T₂-weighted images as source domain inputs to the previous method. In contrast, BlindHarmony is limited in its ability to perform contrast conversion, which stems from its reliance on an image distance function for optimizing images. Still, the BlindHarmonyDiff results reveal limitations, such as the imperfect conversion of detailed structures.

5. Discussion

We introduce BlindHarmonyDiff, a novel 3D blind harmonization framework that leverages an edge-to-image model. Our approach addresses key limitations of existing blind harmonization methods, including inter-slice heterogeneity,

moderate image quality, and poor performance for large domain gaps. BlindHarmonyDiff effectively handles images with large domain gaps and generates high-quality 3D harmonized images, as evidenced by higher PSNR and SSIM values and improved performance in downstream tasks compared to previous methods. Furthermore, results indicate that this 3D processing is advantageous for producing high-quality harmonized images by considering inter-slice information. (see Fig. 5)

To address the GPU memory challenges associated with training the 3D model, previous methods have employed a patch-based approach [6, 14, 49, 50], which involves partitioning 3D images into smaller patches for neural network training. However, these patch-based methods have not simultaneously achieved efficient memory usage and the ability to capture global context. We propose a multi-stride patch training approach that constructs patches at different strides, enabling the model to incorporate global information while maintaining efficient memory usage. We utilize a normalized index-based method for coordinate encoding. Future research directions may explore alternative spatial encoding techniques, such as sinusoidal encoding, to enhance spatial representation. Additionally, advanced downsampling methods (*e.g.*, Gaussian-weighted non-uniform downsampling) could also be investigated in the context of multi-stride patches.

As demonstrated in an ablation study, the edge-to-image model alone cannot effectively harmonize source domain images to the target domain. This limitation can be attributed to two main factors. First, although we attempt to generate a homogeneous edge map from the source domain image through threshold tuning, (See Supplementary material S1) some edge maps may still exhibit heterogeneous features compared to the edge of the target domain image. Second, the edge-to-image model is susceptible to potential hallucinations [1, 25]. The refinement module plays a crucial role in incorporating source domain structural information into the harmonized image, thereby enabling more accurate and robust harmonization. The erroneous outputs of the edge-to-image model are particularly pronounced when dealing with uncommon features such as lesions and hemorrhages (see Fig. 6). Consequently, the refinement module is essential for reliable medical image analysis.

Evaluation of harmonization using traveling subjects with image-level correspondence between harmonized and target domain images is a straightforward approach. However, image fidelity metrics such as PSNR and SSIM have known limitations in capturing all aspects of image quality [34]. Moreover, the evaluation process with traveling subjects is susceptible to errors stemming from imperfect registration or temporal gaps between acquisitions. Therefore, we also conduct evaluations based on downstream tasks.

In our study, we apply our method to a limited sam-

ple of patient data; therefore, further validation with large-scale patient datasets is necessary. Additionally, we select two proof-of-concept downstream tasks that are straightforward to implement. To better analyze the clinical utility of our method, future work should explore its application to a broader range of disease-related downstream tasks.

The application of BlindHarmonyDiff to contrast conversion (*e.g.*, T_2 -weighted image to T_1 -weighted image; see Fig. 7) produces a T_1 -weighted image that retains the edges of the input, but the performance remains limited. This limitation arises from the imperfect edge detection for the T_2 -weighted image, as the threshold tuning was defined based on T_1 -weighted images. Additionally, we cannot apply the refinement module because the correlation between T_1 -weighted and T_2 -weighted images is largely lower than that between two T_1 -weighted images from different domains. Further research is required to effectively model the relationship between different contrasts.

MRI harmonization shares similarities with domain adaptation in neural networks, as both seek to reduce the domain gap in image data. However, a key distinction lies in their focus: harmonization emphasizes image-level correspondence, while domain adaptation prioritizes the performance of the neural network. MRI presents unique challenges compared to other medical imaging modalities (*e.g.*, CT, X-ray), as achieving a homogeneous dataset without contrast variation is difficult due to long scan times and varying vendors, requiring a harmonization process for large dataset construction.

Blind harmonization is particularly advantageous when applying harmonization techniques to unknown source domains or those lacking sufficient training data. For instance, when operating an API service that takes MRI inputs, it can be challenging to identify the domain of the input images. In such cases, blind harmonization can enhance the performance of the API service by effectively handling the input data with domain gaps. However, if sufficient source domain data is available for training, employing a harmonization method optimized for a specific source domain (*e.g.*, DeepHarmony, style transfer; see Fig. 3) may yield superior results.

6. Conclusion

In this study, we proposed BlindHarmonyDiff, a 3D blind harmonization framework leveraging an edge-to-image model to generate high-quality 3D harmonized images with inter-slice consistency. Furthermore, we proposed an efficient 3D patch training scheme with multi-stride patches and a refinement module to effectively suppress hallucination, ensuring practicality and clinical reliability. We have demonstrated excellent performance of our BlindHarmonyDiff in image quality metrics as well as in downstream task-based metrics over prior arts across diverse MR scanners.

References

- [1] Sumukh K Aithal, Pratyush Maini, Zachary C Lipton, and J Zico Kolter. Understanding hallucinations in diffusion models through mode interpolation. *arXiv preprint arXiv:2406.09358*, 2024. 8
- [2] Zeynettin Akkus, Alfiia Galimzianova, Assaf Hoogi, Daniel L Rubin, and Bradley J Erickson. Deep learning for brain mri segmentation: state of the art and future directions. *Journal of Digital Imaging*, 30:449–459, 2017. 1
- [3] Silvia Basaia, Federica Agosta, Luca Wagner, Elisa Canu, Giuseppe Magnani, Roberto Santangelo, Massimo Filippi, Alzheimer’s Disease Neuroimaging Initiative, et al. Automated classification of alzheimer’s disease and mild cognitive impairment using a single mri and deep neural networks. *NeuroImage: Clinical*, 21:101645, 2019. 1
- [4] Vishnu M Bashyam, Jimit Doshi, Guray Erus, Dhivya Srinivasan, Ahmed Abdulkadir, Ashish Singh, Mohamad Habes, Yong Fan, Colin L Masters, Paul Maruff, et al. Deep generative medical image harmonization for improving cross-site generalization in deep learning predictors. *Journal of Magnetic Resonance Imaging*, 55(3):908–916, 2022. 1
- [5] Farzad Beizae, Gregory A Lodygensky, Chris L Adamson, Deanne K Thompson, Jeanie LY Cheong, Alicia J Spittle, Peter J Anderson, Christian Desrosiers, and Jose Dolz. Harmonizing flows: Leveraging normalizing flows for unsupervised and source-free mri harmonization. *Medical Image Analysis*, page 103483, 2025. 1, 2
- [6] Florentin Bieder, Julia Wolleb, Alicia Durrer, Robin Sandkuehler, and Philippe C Cattin. Memory-efficient 3d denoising diffusion models for medical image processing. In *MIDL*, 2023. 1, 2, 3, 8
- [7] Stenzel Cackowski, Emmanuel L Barbier, Michel Dojat, and Thomas Christen. Imunity: a generalizable vae-gan solution for multicenter mr image harmonization. *Medical Image Analysis*, 88:102799, 2023. 2
- [8] John Canny. A computational approach to edge detection. *IEEE TPAMI*, (6):679–698, 1986. 3
- [9] Yuwen Chen, Nicholas Konz, Hanxue Gu, Haoyu Dong, Yaqian Chen, Lin Li, Jisoo Lee, and Maciej A Mazurowski. Contourdiff: Unpaired image translation with contourguided diffusion models. *arXiv preprint arXiv:2403.10786*, 2(3):4, 2024. 2
- [10] Hyungjin Chung, Dohoon Ryu, Michael T McCann, Marc L Klasky, and Jong Chul Ye. Solving 3d inverse problems using pre-trained 2d diffusion models. In *CVPR*, 2023. 1
- [11] James H Cole, Rudra PK Poudel, Dimosthenis Tsagkrasoulis, Matthan WA Caan, Claire Steves, Tim D Spector, and Giovanni Montana. Predicting brain age with deep learning from raw imaging data results in a reliable and heritable biomarker. *NeuroImage*, 163:115–124, 2017. 6, 3
- [12] Blake E Dewey, Can Zhao, Jacob C Reinhold, Aaron Carass, Kathryn C Fitzgerald, Elias S Sotirchos, Shiv Saidha, Jiwon Oh, Dzung L Pham, Peter A Calabresi, et al. Deepharmony: A deep learning approach to contrast harmonization across scanner changes. *Magnetic Resonance Imaging*, 64:160–170, 2019. 1, 2, 4, 5, 6
- [13] Blake E Dewey, Lianrui Zuo, Aaron Carass, Yufan He, Yihao Liu, Ellen M Mowry, Scott Newsome, Jiwon Oh, Peter A Calabresi, and Jerry L Prince. A disentangled latent space for cross-site mri harmonization. In *MICCAI*, 2020. 1, 2
- [14] Zheng Ding, Mengqi Zhang, Jiajun Wu, and Zhuowen Tu. Patched denoising diffusion models for high-resolution image synthesis. In *ICLR*, 2024. 2, 8
- [15] Nicola K Dinsdale, Mark Jenkinson, and Ana IL Namburete. Deep learning-based unlearning of dataset bias for mri harmonisation and confound removal. *NeuroImage*, 228:117689, 2021. 1
- [16] Conor Durkan, Artur Bekasov, Iain Murray, and George Papamakarios. Neural spline flows. *NeurIPS*, 32, 2019. 2
- [17] Jean-Philippe Fortin, Drew Parker, Birkan Tunç, Takanori Watanabe, Mark A Elliott, Kosha Ruparel, David R Roalf, Theodore D Satterthwaite, Ruben C Gur, Raquel E Gur, et al. Harmonization of multi-site diffusion tensor imaging data. *NeuroImage*, 161:149–170, 2017. 1, 2
- [18] Paul Friedrich, Yannik Frisch, and Philippe C Cattin. Deep generative models for 3d medical image synthesis. *arXiv preprint arXiv:2410.17664*, 2024. 1
- [19] Hao Guan, Yunbi Liu, Erkun Yang, Pew-Thian Yap, Dinggang Shen, and Mingxia Liu. Multi-site mri harmonization via attention-guided deep domain adaptation for brain disorder identification. *Medical Image Analysis*, 71:102076, 2021. 1
- [20] Hao Guan, Siyuan Liu, Weili Lin, Pew-Thian Yap, and Mingxia Liu. Fast image-level mri harmonization via spectrum analysis. In *MLMI*, 2022. 4, 5, 6, 2, 3
- [21] Kerstin Hammernik, Teresa Klatzer, Erich Kobler, Michael P Recht, Daniel K Sodickson, Thomas Pock, and Florian Knoll. Learning a variational network for reconstruction of accelerated mri data. *Magnetic Resonance in Medicine*, 79(6):3055–3071, 2018. 1
- [22] Mark Jenkinson, Peter Bannister, Michael Brady, and Stephen Smith. Improved optimization for the robust and accurate linear registration and motion correction of brain images. *NeuroImage*, 17(2):825–841, 2002. 4
- [23] Hwihun Jeong, Heejoon Byun, Dong Un Kang, and Jongho Lee. Blindharmony:” blind” harmonization for mr images via flow model. In *ICCV*, 2023. 1, 2, 4, 5, 6, 3
- [24] Firas Khader, Gustav Müller-Franzes, Soroosh Tayebi Arasteh, Tianyu Han, Christoph Haarbuerger, Maximilian Schulze-Hagen, Philipp Schad, Sandy Engelhardt, Bettina Baeßler, Sebastian Foersch, et al. Denoising diffusion probabilistic models for 3d medical image generation. *Scientific Reports*, 13(1):7303, 2023. 1
- [25] Seunghoi Kim, Chen Jin, Tom Diethe, Matteo Figini, Henry FJ Tregidgo, Asher Mullokandov, Philip Teare, and Daniel C Alexander. Tackling structural hallucination in image translation with local diffusion. In *ECCV*, 2024. 8
- [26] Sergey Korolev, Amir Safiullin, Mikhail Belyaev, and Yulia Dodonova. Residual and plain convolutional neural networks for 3d brain mri classification. In *ISBI*. IEEE, 2017. 1
- [27] Pamela J LaMontagne, Tammie LS Benzinger, John C Morris, Sarah Keefe, Russ Hornbeck, Chengjie Xiong, Elizabeth Grant, Jason Hassenstab, Krista Moulder, Andrei G

- Vlassenko, et al. Oasis-3: longitudinal neuroimaging, clinical, and cognitive dataset for normal aging and alzheimer disease. *medRxiv*, pages 2019–12, 2019. 4, 6, 1
- [28] Suhyeon Lee, Hyungjin Chung, Minyoung Park, Jonghyuk Park, Wi-Sun Ryu, and Jong Chul Ye. Improving 3d imaging with pre-trained perpendicular 2d diffusion models. In *ICCV*, 2023. 1
- [29] Yaron Lipman, Ricky TQ Chen, Heli Ben-Hamu, Maximilian Nickel, and Matthew Le. Flow matching for generative modeling. In *ICLR*, 2023. 1, 3
- [30] Mengting Liu, Piyush Maiti, Sophia Thomopoulos, Alyssa Zhu, Yaqiong Chai, Hosung Kim, and Neda Jahanshad. Style transfer using generative adversarial networks for multi-site mri harmonization. In *MICCAI*, 2021. 1, 2, 4, 5, 6
- [31] Xingchao Liu, Chengyue Gong, and Qiang Liu. Flow straight and fast: Learning to generate and transfer data with rectified flow. In *ICLR*, 2023. 1
- [32] Hengameh Mirzaalian, Lipeng Ning, Peter Savadjiev, Ofer Pasternak, Sylvain Bouix, O Michailovich, Gerald Grant, Christine E Marx, Rajendra A Morey, Laura A Flashman, et al. Inter-site and inter-scanner diffusion mri data harmonization. *NeuroImage*, 135:311–323, 2016. 1
- [33] Gourav Modanwal, Adithya Vellal, Mateusz Buda, and Maciej A Mazurowski. Mri image harmonization using cycle-consistent generative adversarial network. In *Medical Imaging: Computer-Aided Diagnosis*, pages 259–264. SPIE, 2020. 1, 2, 4, 5, 6
- [34] Jim Nilsson and Tomas Akenine-Möller. Understanding ssim. *arXiv preprint arXiv:2006.13846*, 2020. 8
- [35] László G Nyúl and Jayaram K Udupa. On standardizing the mr image intensity scale. *Magnetic Resonance in Medicine*, 42(6):1072–1081, 1999. 1, 2
- [36] László G Nyúl, Jayaram K Udupa, and Xuan Zhang. New variants of a method of mri scale standardization. *IEEE TMI*, 19(2):143–150, 2000. 2
- [37] Emanuel Parzen. On estimation of a probability density function and mode. *The Annals of Mathematical Statistics*, 33(3): 1065–1076, 1962. 7
- [38] Raymond Pomponio, Guray Erus, Mohamad Habes, Jimit Doshi, Dhivya Srinivasan, Elizabeth Mamourian, Vishnu Bashyam, Ilya M Nasrallah, Theodore D Satterthwaite, Yong Fan, et al. Harmonization of large mri datasets for the analysis of brain imaging patterns throughout the lifespan. *NeuroImage*, 208:116450, 2020. 1, 2
- [39] Olaf Ronneberger, Philipp Fischer, and Thomas Brox. U-net: Convolutional networks for biomedical image segmentation. In *MICCAI*, 2015. 4, 6, 1, 2
- [40] Tim Salimans and Jonathan Ho. Progressive distillation for fast sampling of diffusion models. In *ICLR*, 2022. 1
- [41] Christian Salvatore, Antonio Cerasa, Isabella Castiglioni, F Gallivanone, A Augimeri, M Lopez, G Arabia, M Morelli, MC Gilardi, and A Quattrone. Machine learning on brain mri data for differential diagnosis of parkinson’s disease and progressive supranuclear palsy. *Journal of Neuroscience Methods*, 222:230–237, 2014. 1
- [42] Russell T Shinohara, Elizabeth M Sweeney, Jeff Goldsmith, Navid Shiee, Farrah J Mateen, Peter A Calabresi, Samson Jarso, Dzung L Pham, Daniel S Reich, Ciprian M Crainiceanu, et al. Statistical normalization techniques for magnetic resonance imaging. *NeuroImage: Clinical*, 6:9–19, 2014. 1, 2
- [43] Russell T Shinohara, Jiwon Oh, Govind Nair, Peter A Calabresi, Christos Davatzikos, Jimit Doshi, Roland G Henry, Gloria Kim, Kristin A Linn, Nico Papinutto, et al. Volumetric analysis from a harmonized multisite brain mri study of a single subject with multiple sclerosis. *American Journal of Neuroradiology*, 38(8):1501–1509, 2017. 1, 2
- [44] Stephen M Smith. Fast robust automated brain extraction. *Human Brain Mapping*, 17(3):143–155, 2002. 5
- [45] Bowen Song, Jason Hu, Zhaoxu Luo, Jeffrey A Fessler, and Liyue Shen. Diffusionblend: Learning 3d image prior through position-aware diffusion score blending for 3d computed tomography reconstruction. In *ICML*, 2024. 1
- [46] Yang Song, Prafulla Dhariwal, Mark Chen, and Ilya Sutskever. Consistency models. In *ICML*, 2023. 1
- [47] Mahbaneh Eshaghzadeh Torbati, Davneet S Minhas, Charles M Laymon, Pauline Maillard, James D Wilson, Chang-Le Chen, Ciprian M Crainiceanu, Charles S DeCarli, Seong Jae Hwang, and Dana L Tudorascu. Mispel: A supervised deep learning harmonization method for multi-scanner neuroimaging data. *Medical Image Analysis*, 89:102926, 2023. 1
- [48] Tianren Wang, Teng Zhang, Liangchen Liu, Arnold Wiliem, and Brian Lovell. Cannygan: Edge-preserving image translation with disentangled features. In *ICIP*, 2019. 2
- [49] Zhendong Wang, Yifan Jiang, Huangjie Zheng, Peihao Wang, Pengcheng He, Zhangyang Wang, Weizhu Chen, Mingyuan Zhou, et al. Patch diffusion: Faster and more data-efficient training of diffusion models. *NeurIPS*, 36, 2023. 2, 3, 8
- [50] Jaeyeon Yoon, Enhao Gong, Itthi Chatnuntawech, Berkin Bilgic, Jingu Lee, Woojin Jung, Jingyu Ko, Hosan Jung, Kavin Setsompop, Greg Zaharchuk, et al. Quantitative susceptibility mapping using deep neural network: Qsmnet. *NeuroImage*, 179:199–206, 2018. 1, 8
- [51] Hongye Zeng, Ke Zou, Zhihao Chen, Rui Zheng, and Huazhu Fu. Reliable source approximation: Source-free unsupervised domain adaptation for vestibular schwannoma mri segmentation. In *MICCAI*, 2024. 2
- [52] Yongyue Zhang, Michael Brady, and Stephen Smith. Segmentation of brain mr images through a hidden markov random field model and the expectation-maximization algorithm. *IEEE TMI*, 20(1):45–57, 2001. 6
- [53] Xiaomei Zhao, Yihong Wu, Guidong Song, Zhenye Li, Yazhuo Zhang, and Yong Fan. A deep learning model integrating fcns and crfs for brain tumor segmentation. *Medical Image Analysis*, 43:98–111, 2018. 1
- [54] Jun-Yan Zhu, Taesung Park, Phillip Isola, and Alexei A Efros. Unpaired image-to-image translation using cycle-consistent adversarial networks. In *ICCV*, pages 2223–2232, 2017. 2
- [55] Lianrui Zuo, Blake E Dewey, Yihao Liu, Yufan He, Scott D Newsome, Ellen M Mowry, Susan M Resnick, Jerry L Prince, and Aaron Carass. Unsupervised mr harmonization by learning disentangled representations using information bottleneck theory. *NeuroImage*, 243:118569, 2021. 2

Efficient and robust 3D blind harmonization for large domain gaps

Supplementary Material

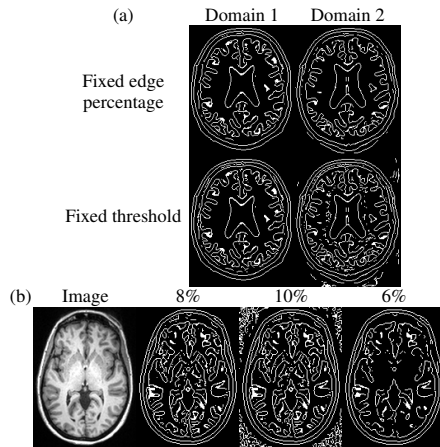


Figure S1. Threshold test

S1. Threshold of Canny edge detection

Canny edge detection can be parameter-sensitive. However, we chose this method for its easy implementation and reproducibility across various domains. To address the parameter sensitivity, we employ a fixed edge percentage approach rather than a fixed threshold. Figure S1a demonstrates that using a fixed percentage yields more consistent edge maps across different domains than a fixed threshold does.

We empirically determined 8% edge, because it provides good edge detection for brain images, as illustrated in the Figure S1b. Although this threshold selection is somewhat heuristic, it produces reliable edge maps for brain structures across our dataset. We recognize that this approach might occasionally result in inconsistent edge detection and produce poor edge-to-image model output (even inferior to the one without harmonization). However, as noted in the Discussion, the refinement module is designed to mitigate such inconsistencies.

S2. Dataset description

The BlindHarmonyDiff framework presented in this study was trained and evaluated using the OASIS3 dataset [27], with a target domain comprising images acquired on a Siemens TIM Trio 3T MR scanner. For the source domain, images from four additional scanners were employed: Siemens Sonata 1.5T, Siemens BioGraph mMR PET-MR 3T, Siemens Vision 1.5T, and Siemens Magnetom Vida 3T MR. All images underwent resampling to a uniform resolution of $1.2 \times 1.2 \times 1.25$ mm (matrix size: $144 \times 208 \times 92$) and were subjected to percentile-based min-max normalization (1st-99th) at the subject level. Table S1 presents detailed

acquisition parameters for each scanner. For target domain training, encompassing edge-to-image model training and downstream task networks training, the dataset was partitioned into train/validation/test sets comprising 717, 29, and 135 subjects, respectively.

S3. Implementation details

S3.1. Edge-to-image model

The 3D edge-to-image model was trained on cubic patches of size $64 \times 64 \times 64$ with a batch size of 8, using 2 NVIDIA Quadro RTX 8000 GPUs. The model was optimized using the Adam optimizer with an L2 loss function and a fixed learning rate of 0.00005 for 150,000 steps.

The architecture is based on a 3D U-Net [39], with five input channels: a grayscale noise channel, a conditional grayscale edge channel, and three positional coordinate channels. The output is a single grayscale channel. The first layer has 64 channels, with depth multipliers of $\{1, 2, 4, 8\}$ applied at successive layers. Each block includes two 3D convolution layers, RMS normalization, and SiLU activation. Downsampling is performed via resampling, where spatial blocks are reorganized into the channel dimension, while upsampling combines nearest-neighbor interpolation and convolution. Skip connections transfer encoder features directly to the decoder, preserving spatial details.

Data augmentation includes random flipping along the x, y, and z axes to increase the diversity of the training data. Multi-stride patches were applied during training to capture multi-scale features, enabling the model to effectively learn both local and global contexts.

During the sampling process, the model used a step size of 16. The ordinary differential equation solver employed the midpoint method, with both absolute and relative error tolerances set to 0.00005.

S3.2. DeepHarmony

The 3D U-Net [39] architecture was employed for the implementation of DeepHarmony [12]. The network comprises 4 Down blocks and 4 Up blocks, with each block consisting of two sequential combinations of a convolution layer ($5 \times 5 \times 5$), batch normalization, and leaky-ReLU activation. Maxpooling is utilized in the Down blocks, while transpose convolution is employed in the Up blocks. The U-Net also incorporates skip connections. Training was conducted using L1 loss and the SGD optimizer with a learning rate of 0.001. The checkpoint exhibiting the best validation loss was selected for evaluation. The dataset size varies by domain, as detailed in Table S1.

	Target domain		Source domain		
Manufacturer	Siemens	Siemens	Siemens	Siemens	Siemens
Scanner version	TIM Trio	Sonata	BioGraph mMR	Vision	Magnetom Vida
Magnetic field strength (T)	3	1.5	3	1.5	3
Matrix size	176×256×256	160×256×256	176×240×256	128×256×256	176×240×256
Resolution (mm^3)	1×1×1	1×1×1	1.2×1.05×1.05	1.25×1×1	1.2×1.05×1.05
TR/TI (s)	2.4/1	1.9/1.1	2.3/0.9	9.7/unknown	2.3/0.9
TE (ms)	3.16	3.93	2.95	4.0	2.95
Flip angle (°)	8	15	9	10	9
Paired data (train/val)	-	20/1	190/7	67/6	47/4
Test subject (image-level)	-	7	30	12	10
Test subject (downstream)	-	8	134	25	54

Table S1. Representative scan parameters for various domains in the OASIS3 dataset are presented. A single data domain may encompass multiple parameter configurations. The ‘Paired data’ row indicates the size of the dataset used for training DeepHarmony and the style transfer network.

		Sonata 1.5T		BioGraph 3T		Vision 1.5T		Magnetom Vida 3T	
	Blind	SSIM(↑)	PSNR(↑)	SSIM(↑)	PSNR(↑)	SSIM(↑)	PSNR(↑)	SSIM(↑)	PSNR(↑)
Source domain		0.795	17.3	0.808	18.2	0.534	12.2	0.780	16.0
BlindHarmonyDiff (ours)	O	0.873	21.2	0.819	20.9	0.611	16.5	0.814	19.5
BlindHarmony [23]	O	0.782	17.4	0.810	18.9	0.578	14.3	0.783	16.5
SSIMH [20]	O	0.734	13.5	0.701	14.2	0.496	12.6	0.709	13.7
Histogram matching	O	0.765	14.5	0.780	16.0	0.566	14.0	0.772	15.4

Table S2. Quantitative assessment using PSNR and SSIM metrics in 2D processing case, calculated relative to the target domain images.

	Sonata 1.5T		BioGraph 3T		Vision 1.5T		Magnetom Vida 3T	
Edge-to-image model	SSIM(↑)	PSNR(↑)	SSIM(↑)	PSNR(↑)	SSIM(↑)	PSNR(↑)	SSIM(↑)	PSNR(↑)
Conditional	0.908	23.4	0.862	23.3	0.697	19.3	0.851	21.3
Unconditional	0.830	21.6	0.765	21.5	0.640	19.3	0.770	20.4
None	0.769	19.2	0.764	20.7	0.630	18.9	0.750	19.7

Table S3. Quantitative ablation studies demonstrate the superiority of the full BlindHarmonyDiff framework incorporating the conditional edge-to-image model. This configuration consistently outperforms the case employing the unconditional edge-to-image model or the case without the edge-to-image model.

S3.3. Style transfer

The style transfer network employed a 2D paired CycleGAN architecture [54]. The generator network comprises 2 convolutional layers with instance normalization and ReLU activation, followed by 9 residual blocks, and concludes with 3 convolutional layers with instance normalization and ReLU activation. Each residual block incorporates a residual connection consisting of 2 convolutional layers with instance normalization and ReLU activation. The discriminator is composed of 5 convolutional layers, 4 leaky ReLU activations, and 4 instance normalization layers. The CycleGAN training objective incorporates identity loss, cycle consistency loss, and adversarial loss. The training was conducted for a maximum of 200 epochs using the Adam optimizer with a learning rate of 0.0002. The dataset size varies by domain, as detailed in Table S1.

S3.4. BlindHarmony

For training the normalizing flow, we adopted the Neural Spline Flow (NSF) architecture [16] with rational quadratic

(RQ) spline coupling layers. The majority of hyperparameters were set to match those used in the original NSF paper for ImageNet experiments. Specifically, we set the tail bound B to 3 and the number of bins K for RQ spline coupling layers to 8. We implemented a multiscale architecture akin to Glow, with each network layer comprising 7 transformation steps: an actnorm layer, an invertible 1×1 convolution, an RQ spline coupling transform, and another 1×1 convolution. The network consists of 4 layers, resulting in 28 coupling transformation steps. The subnetworks parameterizing the RQ splines incorporate 3 residual blocks and batch normalization layers. We optimized the parameters using an Adam optimizer with an initial learning rate of 0.0005 and cosine annealing, iterating up to 10K steps.

S3.5. Tissue segmentation network

The 2D U-Net [39] architecture was employed for implementing the tissue segmentation network. The network comprises 4 Down blocks and 4 Up blocks. Each Down block consists of a maxpooling layer (2×2), followed by

	2D		3D	
	SSIM(\uparrow)	PSNR(\uparrow)	SSIM(\uparrow)	PSNR(\uparrow)
Whole image	0.813	24.0	-	-
Multi-stride patch	0.817	24.1	0.920	27.5
Simple patch	0.809	23.9	0.905	26.9

Table S4. Comparison between multi-stride patch training and simple patch training.

two sequences of convolution layer (3×3), batch normalization, and ReLU activation. Up blocks are composed of a bilinear upsampling layer (2×2), followed by two sequences of convolution layer (3×3), batch normalization, and ReLU activation. The U-Net incorporates skip connections between corresponding Down and Up blocks. The training was conducted using L1 loss and the Adam optimizer with a learning rate of 0.0001. The checkpoint exhibiting the best validation loss was selected for evaluation.

S3.6. Age prediction network

A 3D CNN architecture similar to that proposed in [11] was implemented for age prediction. The network comprises 5 repeated blocks, each consisting of a ($3 \times 3 \times 3$) convolutional layer with stride 1, followed by ReLU activation, another ($3 \times 3 \times 3$) convolutional layer with stride 1, a 3D batch-normalization layer, ReLU activation, and a ($2 \times 2 \times 2$) max-pooling layer with stride 2. The number of feature channels is initialized at eight in the first block and doubles after each max-pooling operation to derive a rich representation of the brain structure. The final age prediction is obtained through a fully connected layer, mapping the output of the last block to a single value. Training was conducted using L1 loss and the SGD optimizer with a learning rate of 0.0001. The model checkpoint exhibiting the best validation loss was selected for evaluation.

S4. Additional test

S4.1. Evaluation of multi-stride patch in 2D

To assess the effectiveness of multi-stride patch training, we conducted experiments in both 2D and 3D scenarios. For 2D cases, we compared whole image training, multi-stride patch training, and simple patch training. In 3D cases, we evaluated multi-stride and simple patch training. PSNR and SSIM metrics were calculated relative to the original image to quantify performance.

Our experimental results (Table S4) demonstrate that multi-stride patch training consistently outperforms simple patch training in both 2D and 3D scenarios. Notably, in 2D cases, multi-stride patch training achieved higher PSNR and SSIM values than even whole-image training. These results highlight the ability of multi-stride patch training to enhance image quality and structural similarity, underscoring its effectiveness.

S4.2. Evaluation of harmonization in 2D

We compared the result when the processing is based on 2D (*i.e.*, slice-wise calculation). BlindHarmonyDiff was implemented using a 2D rectified flow model trained at the slice level, without utilizing patch-based training. The refinement module employed slice-wise normalized cross-correlation calculations. For SSIMH [20], the approach involved averaging whole slices of target domain images and replacing the low-frequency components of source domain images with these averaged target domain images using a 2D discrete cosine transform. Histogram matching was performed by storing the histogram of target domain images and matching the source domain image histogram to the target domain histogram at the slice level. Metrics were calculated slice-wise, while the 2D metrics in Table 3 were computed for the whole 3D brain volume.

Quantitative analysis results (Table S2) demonstrate that the overall performance trends are consistent with the 3D case. BlindHarmonyDiff outperforms other blind harmonization techniques, including BlindHarmony [23], histogram matching, and SSIMH [20], in both PSNR and SSIM metrics. Notably, the normalizing flow-based BlindHarmony method showed superior performance compared to SSIMH and histogram matching, which aligns with findings reported by previous study [23].

S4.3. Ablation test: the case without edge-to-image model

To evaluate the contribution of the edge-to-image model in harmonization, we conducted a comparative analysis of three configurations: BlindHarmonyDiff with the proposed conditional edge-to-image model, BlindHarmonyDiff with an unconditional edge-to-image model, and BlindHarmonyDiff without an edge-to-image model. For the unconditional edge-to-image model variant, we did not train a separate model but instead input random edge conditions when generating input for the refinement module. In the case without an edge-to-image model, we applied only the refinement module to the averaged image from the target domain training dataset.

Quantitative analysis (Table S3) demonstrates that the original BlindHarmonyDiff, incorporating the conditional edge-to-image model, outperforms both the unconditional variant and the version without an edge-to-image model. While the refinement module does enforce some structural information from the source domain image, the initial starting point provided by the edge-to-image model proves crucial for achieving high-quality harmonization. These results underscore the importance of the conditional edge-to-image model in the BlindHarmonyDiff framework for effective image harmonization.

S5. Visual examples

Exemplary images of the image level evaluation and the downstream task evaluation are illustrated in Figures [S2](#) and [S3](#).

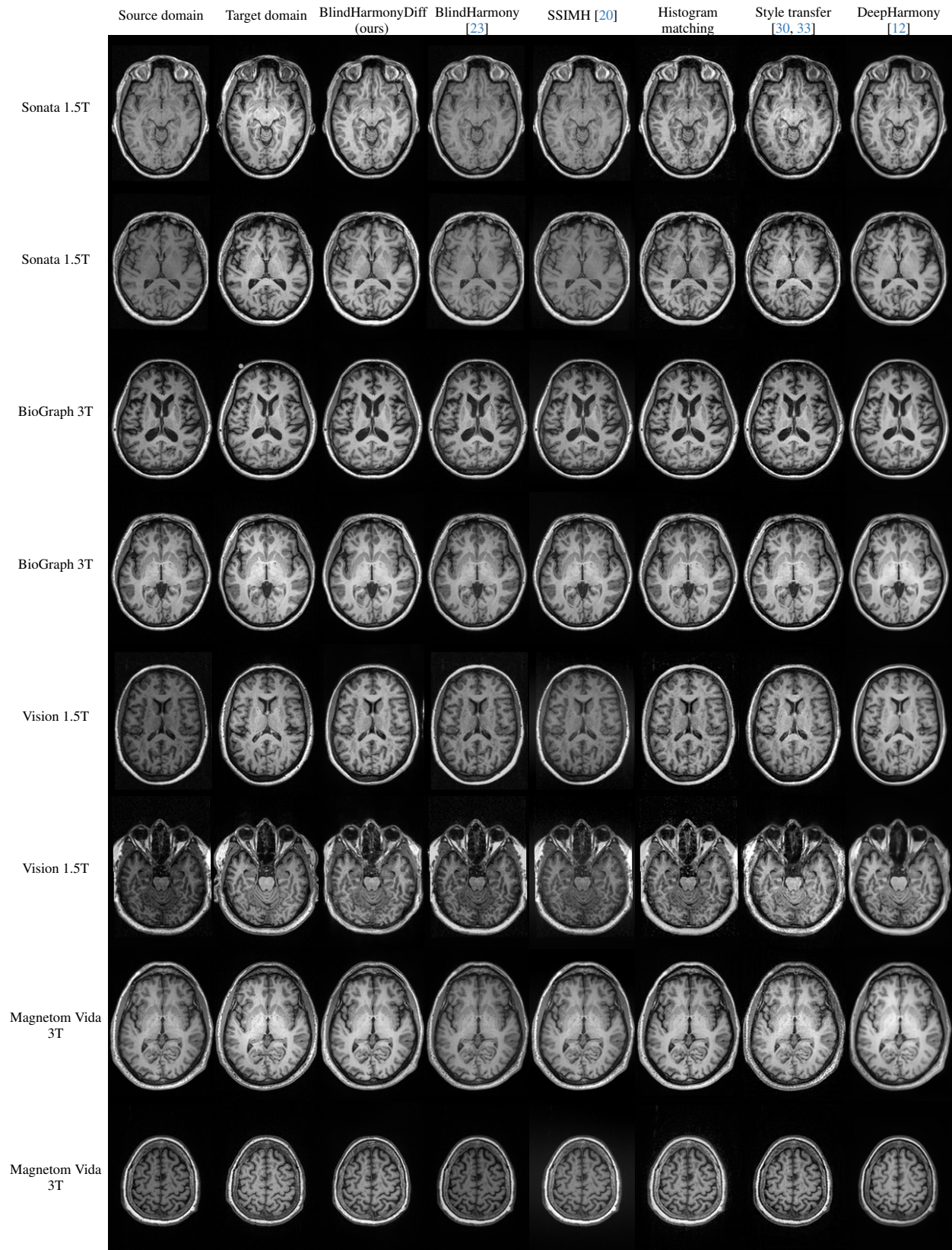


Figure S2. Visual comparison of harmonization results on traveling subjects, demonstrating the effectiveness of BlindHarmonyDiff against the other blind harmonization methods.

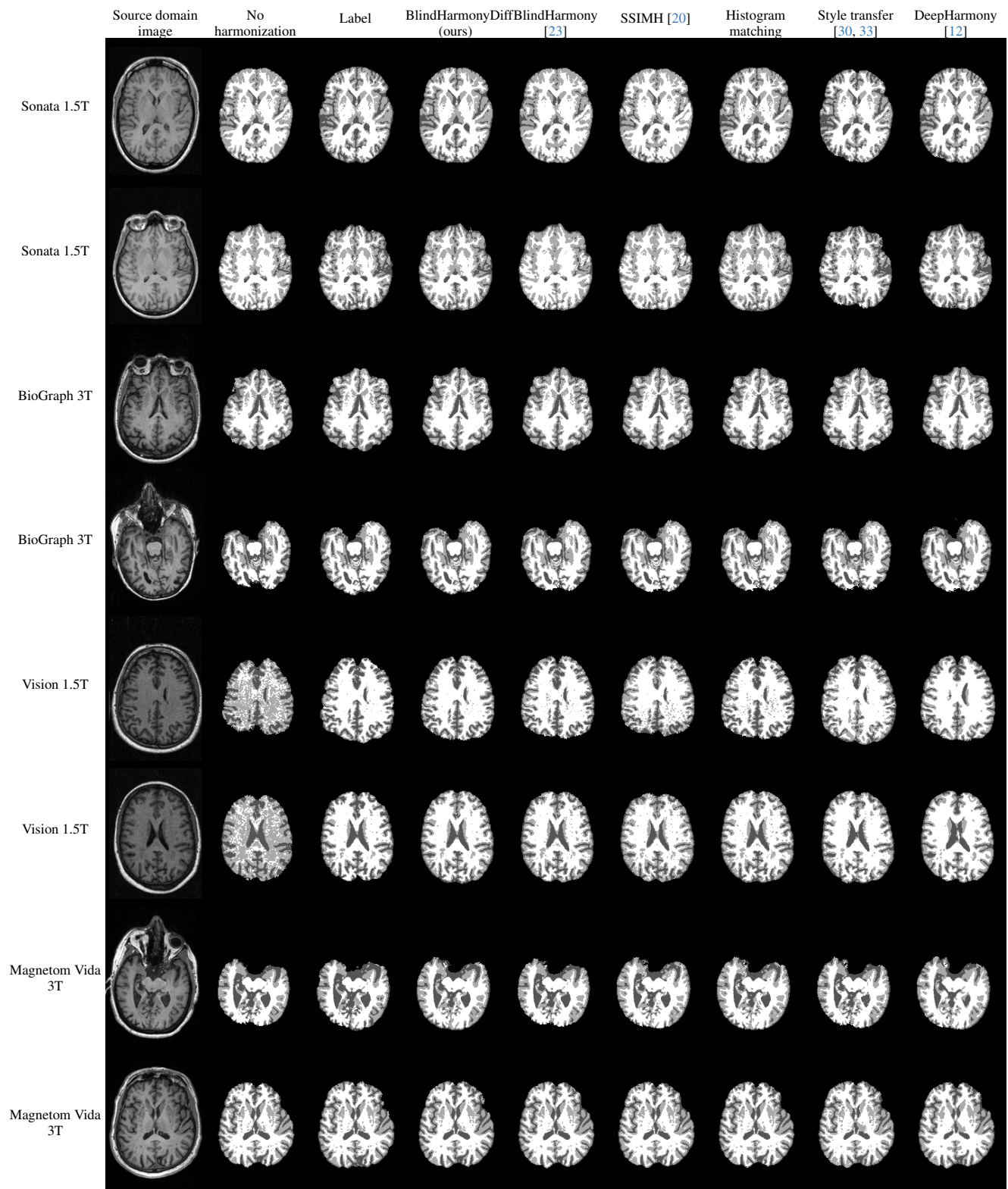


Figure S3. Tissue segmentation results for the various harmonization methods, with the segmentation network trained on the target domain data. Each column represents a different harmonization approach applied to the input images.